

## Evaluation of model-based deformation correction in image-guided liver surgery via tracked intraoperative ultrasound

Logan W. Clements  
Jarrod A. Collins  
Jared A. Weis  
Amber L. Simpson  
Lauryn B. Adams  
William R. Jarnagin  
Michael I. Miga

# Evaluation of model-based deformation correction in image-guided liver surgery via tracked intraoperative ultrasound

Logan W. Clements,<sup>a,\*</sup> Jarrod A. Collins,<sup>a</sup> Jared A. Weis,<sup>a</sup> Amber L. Simpson,<sup>b</sup> Lauryn B. Adams,<sup>b</sup> William R. Jarnagin,<sup>b</sup> and Michael I. Miga<sup>a</sup>

<sup>a</sup>Vanderbilt University, Department of Biomedical Engineering, 5824 Stevenson Center, Nashville, Tennessee 37232, United States

<sup>b</sup>Memorial Sloan-Kettering Cancer Center, Department of Surgery, 1275 York Avenue, New York, New York 10065, United States

**Abstract.** Soft-tissue deformation represents a significant error source in current surgical navigation systems used for open hepatic procedures. While numerous algorithms have been proposed to rectify the tissue deformation that is encountered during open liver surgery, clinical validation of the proposed methods has been limited to surface-based metrics, and subsurface validation has largely been performed via phantom experiments. The proposed method involves the analysis of two deformation-correction algorithms for open hepatic image-guided surgery systems via subsurface targets digitized with tracked intraoperative ultrasound (iUS). Intraoperative surface digitizations were acquired via a laser range scanner and an optically tracked stylus for the purposes of computing the physical-to-image space registration and for use in retrospective deformation-correction algorithms. Upon completion of surface digitization, the organ was interrogated with a tracked iUS transducer where the iUS images and corresponding tracked locations were recorded. Mean closest-point distances between the feature contours delineated in the iUS images and corresponding three-dimensional anatomical model generated from preoperative tomograms were computed to quantify the extent to which the deformation-correction algorithms improved registration accuracy. The results for six patients, including eight anatomical targets, indicate that deformation correction can facilitate reduction in target error of ~52%. © 2016 Society of Photo-Optical Instrumentation Engineers (SPIE) [DOI: [10.1117/1.JMI.3.1.015003](https://doi.org/10.1117/1.JMI.3.1.015003)]

Keywords: biomechanical modeling; image-guided surgery; open liver surgery; tracked ultrasound; clinical evaluation.

Paper 15182PR received Sep. 9, 2015; accepted for publication Feb. 11, 2016; published online Mar. 23, 2016.

## 1 Introduction

For the successful translation of image-guided surgery approaches to soft-tissue environments, the problem of intraoperative soft-tissue deformation needs to be overcome. Similar to the well-documented brain shift experienced during neurosurgical procedures, intraoperative soft-tissue deformation imposed after laparotomy in open hepatic resections is the primary source of error in current image-guided liver surgery (IGLS) systems. Several studies quantifying the extent of soft-tissue liver deformations have been reported. Heizmann et al.<sup>1</sup> visualize soft-tissue deformation via rendered vascular structure tracking within an intraoperative CT (iCT) environment to include measurements of volumetric changes in anatomical regions during the surgical procedure. Cash et al.<sup>2</sup> made some initial measurements of soft-tissue deformation during IGLS procedures. While informative, the work by Clements et al.<sup>3</sup> made a much more extensive systematic study of the trends in deformation by looking at the surface-fits of laser range data of the organ surface to its preoperative counterpart over 12 open resection cases. Interestingly, the work also performed an interpatient registration that suggested some similarity exists in imposed deformation among similar procedure types.

Given the fact that intraoperative soft-tissue deformation can limit the utility of preoperative tomographic imaging for surgical

guidance, numerous avenues have been suggested to aid in the compensation for the experienced soft-tissue deformation, including the use of intraoperative tomography and ultrasound. However, intraoperative magnetic resonance and iCT imaging equipment is cumbersome, overly expensive for a majority of hospital budgets, and not presently considered standard for care in open liver procedures.<sup>4,5</sup> Additionally, intraoperative two-dimensional (2-D) ultrasound (iUS) provides low signal-to-noise, sparse images of the patient's anatomy. Studies have been performed to evaluate the utility of three-dimensional (3-D) iUS for navigated resection of liver tumors, but such a system is limited by the fact that some lesions cannot be identified via iUS imaging.<sup>6</sup> Ultimately, the ideal image-guidance modality is to update the high-contrast, high-resolution preoperative tomograms to match the intraoperative presentation.

### 1.1 Related Work

A number of previous studies have focused on the development and validation of the model-based deformation-compensation methods driven by sparse organ surface data for IGLS. A number of previous studies have focused on the development and validation of the biomechanical model-based deformation compensation methods driven by sparse organ surface data for IGLS. The initial work by Miga et al.<sup>7</sup> proposed the use of laser range scanner (LRS) data to drive a biomechanical model of the liver

\*Address all correspondence to: Logan W. Clements, E-mail: [logan.clements@vanderbilt.edu](mailto:logan.clements@vanderbilt.edu)

to correct for nonrigid alignment errors. That initial work used surface residual-error metrics to evaluate the correction. Cash et al.<sup>8</sup> enhanced that work by proposing an incremental approach to generate more natural deformations and capture deformation trajectories. This work was investigated using a phantom liver model experiencing realistic scale deformations and contained a set of six subsurface tumor targets. The work by Dumpuri et al.<sup>9</sup> described an approach to generate a boundary condition sets that were extrapolated closest-point boundary conditions in regions outside the immediate laser range area using a surface Laplacian approach equation driven by the intraoperative sparse surface and preoperative organ model data. This method was investigated using both an anthropomorphic liver phantom containing 48 subsurface steel-bead targets and clinical data where surface closest-point residual-error metrics were employed. In recent developments, Rucker et al.<sup>10</sup> proposed a model-based nonrigid registration technique that involved the use of a Levenberg–Marquardt optimization framework to estimate parameters of a bivariate polynomial support surface that acted to specify surface displacements. Similar to the work of Dumpuri et al.,<sup>9</sup> the method was investigated using two anthropomorphic liver phantoms with subsurface targets as well as clinical data where the surface residuals provided the target error metric.

Other approaches have focused on the use of spline-based nonrigid registration techniques to compensate for surgical deformation. Lange et al.<sup>11</sup> used tracked 3-D iUS to generate a series of vessel landmarks to drive a spline-based deformable registration algorithm. The algorithm was investigated using the vessel landmarks as well as a vessel centerline closest-point distance metric. Nakamoto et al.<sup>12</sup> has described a method to model respiratory motion and liver deformation using a freehand 3-D ultrasound system in laparoscopic procedures. The validation experiments for this work were performed via a porcine model and the error quantification involved a “leave-N-out” cross validation. Spline-based nonrigid registration techniques are limited in that the deformation fields provided may only be valid over the region for which data have been acquired which could lead to spurious results outside the region of interest. The strength of a biomechanical model-based algorithm lies in the ability to compute full organ displacement fields from sparse intraoperative data.

It is clear from the above work, open liver surgery represents a challenging environment for validation with much of the work above being investigated via liver phantoms equipped with

subsurface targets, animal experiments, or by surface-error metrics in clinical datasets. The acquisition of a series of clinical data that provides both sparse organ surface characterization as well as subsurface target digitization is a critical step for the refinement and validation of the proposed biomechanical model-based deformation-correction techniques.

## 1.2 Objective

The primary objective of this work is to define a validation procedure of a model-based deformation compensation algorithm driven by sparse organ surface data using tracked iUS acquisitions of subsurface anatomical landmarks acquired during clinical procedures. A subsurface target error metric can be computed between the contours of anatomical structures delineated in tracked iUS and corresponding 3-D anatomical models generated from preoperative image sets. For this work, the performance of two different biomechanical model-based deformation-correction techniques will be evaluated.

## 2 Methods

The proposed deformation-correction clinical validation technique involves three steps: (1) clinical data collection using a surgical navigation system equipped with ultrasound tracking functionality, (2) retrospective deformation correction using the intraoperatively acquired liver surface digitization to drive the algorithm, and (3) retrospective quantification of the efficacy of deformation correction based on subsurface anatomical landmarks that can be localized in the tracked iUS images as well as the preoperative tomograms.

### 2.1 Clinical Data Collection

For this study, a series of clinical data have been acquired for six patients undergoing open liver resection at Memorial Sloan-Kettering Cancer Center. The patients provided written consent and were enrolled in an ongoing study that has been approved by the Memorial Sloan-Kettering Cancer Center Institutional Review Board. A summary of the demographic, pathology, and surgical procedure information for the six patients is shown in Table 1.

#### 2.1.1 Preoperative image processing

Standard contrast-enhanced CT images were acquired for all patients prior to the surgical procedure for radiological

**Table 1** A summary of the demographic, pathology, and surgical procedure information for the patients enrolled in the Institutional review board-approved clinical study at Memorial Sloan-Kettering Cancer Center. The study population included six patients for which eight anatomical feature targets were digitized intraoperatively with tracked 2-D iUS.

Patient	Sex	Age	Weight (kg)	Height (cm)	Pathology	Resection
1	F	36	66.2	160	Metastatic colorectal cancer	N/A
2	M	56	68.9	160	Intrahepatic cholangiocarcinoma	Right lobectomy
3	F	36	81.1	168	Intrahepatic cholangiocarcinoma	Left lobectomy
4	M	54	93.4	186	Metastatic colorectal cancer	Left lobectomy and caudate lobectomy
5	M	76	55.0	159	Metastatic colorectal cancer	Right lobectomy
6	M	45	78.0	183	Metastatic colorectal cancer	Segmentectomy (II) and 2× Wedge (III)

evaluation and surgical planning processes. Prior to the surgical procedure, 3-D anatomical models of the liver, tumor(s), and vasculature structures were generated from the preoperative tomograms using surgical planning software (Scout™ Liver, Analogic Corporation, Peabody, Massachusetts). A summary of the methods used in the preoperative planning software has been provided by Li et al.<sup>13</sup> and an evaluation of the clinical impact of the software has been performed by DuBray et al.<sup>14</sup> Upon completion of the processing, the preoperative tomographic data and associated anatomical models were then imported into a surgical navigation system (Explorer™ Liver, Analogic Corporation, Peabody, Massachusetts) for use during the open-resection procedure.

### 2.1.2 Intraoperative data collection

After laparotomy and liver mobilization, the anterior liver surface was digitized using both a tracked LRS and an optically tracked stylus. An image of the tracked LRS device and the Explorer™ interface used for the manual stylus-based surface acquisition are shown in Fig. 1. The LRS device is used to acquire an initial dense scan of the liver surface within line of sight via the laparotomy incision. Further, a brief apneic period, initialized at end-inspiration, is used to minimize motion artifacts in the scan due to respiration. Based on the work of Cash et al.<sup>2</sup>, hepatic motion due to respiration in open liver surgery displays a periodicity that supports the use of apneic periods at similar points in the respiratory cycle to facilitate data collection that is minimally impacted by respiratory motion. The LRS device used in this study has been characterized by Pheiffer et al.<sup>15</sup>

In addition to the LRS surface digitization, a surface acquisition also performed via manually swabbing the surface of the organ with an optically tracked stylus. In addition to acquiring the liver surface, a series of anatomical features including the umbilical fissure, falciform ligament, and inferior ridges are also acquired for the purposes of driving the salient feature rigid surface registration used within the Explorer™ Liver guidance system.<sup>17</sup> As with the LRS acquisition, a brief apneic period was used to compensate for respiratory motion.

After qualitative evaluation of the registration within the guidance display, the clinician proceeded to interrogate the organ with the tracked iUS transducer (shown in Fig. 2). The Explorer™ Liver navigation system is equipped with a tracked rigid body attachment designed for the Aloka T-probe (Hitachi Aloka Medical Ltd., Wallingford, Connecticut). The tracked

ultrasound system was calibrated using the method described by Chen et al.<sup>18</sup> and clinical experience with the tracked iUS equipped navigation system has been described by Kingham et al.<sup>16</sup> During the surgical procedure, the clinician utilized the tracked iUS to image anatomical features that could be reliably identified within the preoperative tomograms. During the interrogation, iUS image screen captures and corresponding tracked locations of the transducer were recorded for retrospective evaluation.

## 2.2 Deformation-correction Methods

The deformation-correction methods that were evaluated in this study have been described previously by Dumpuri et al.<sup>9</sup> and Rucker et al.<sup>10</sup> To provide an overview, both methods are biomechanical model-based techniques driven by sparse surface data of the organ collected intraoperatively. The method described by Dumpuri et al. (Algorithm 1) is based on the fact that the rigid alignment between the intraoperative sparse organ surface and the preoperative model surface provides an insight into the surface displacements that are reflected by the intraoperative surface deformation. Given that intraoperative organ surface digitizations are sparse in nature, the algorithm uses a surface Laplacian to extrapolate the closest-point distance measurements and generate a realistic set of surface displacement boundary conditions. The method described by Rucker et al. (Algorithm 2) utilizes a parameterized “support surface” to reflect the impact of the liver mobilization and “packing” procedure that occurs after laparotomy. The support surface is described by a bivariate polynomial that specifies a series of surface displacements. An optimization framework is then used to determine the optimal parameters for the support surface such that the residual error between the intraoperative sparse surface digitization and the deformed liver surface, generated from preoperative images, is minimized.

### 2.2.1 Biomechanical model

The underlying tissue-deformation model begins with the assumption that the liver is an isotropic solid with a linear stress-strain relationship as in previous studies.<sup>7–9</sup> The equation for a linear-elastic 3-D solid at static equilibrium is

$$\nabla \cdot \sigma = B, \quad (1)$$

where  $\sigma$  represents the stress tensor and  $B$  represents the body forces acting on the object. Given Hooke’s law, a series of

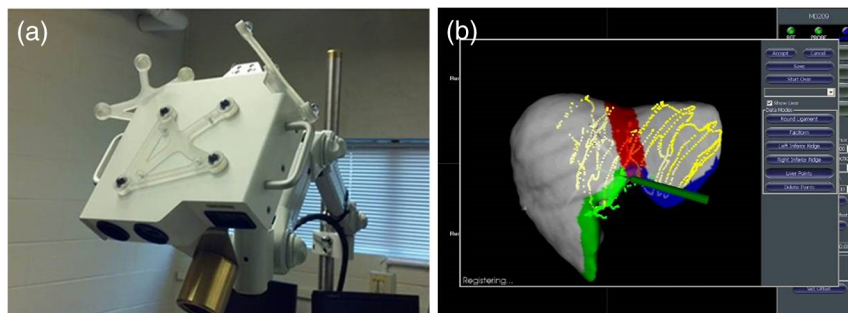


**Fig. 1** (a) The tracked LRS device used for organ surface acquisition during the study. (b) The manual surface swabbing interface within the Explorer™ Liver navigation system highlighting a surface alignment generated from the stylus-based digitization. Note that the images shown were initially included in the works of Pheiffer et al.<sup>15</sup> and Kingham et al.<sup>16</sup>



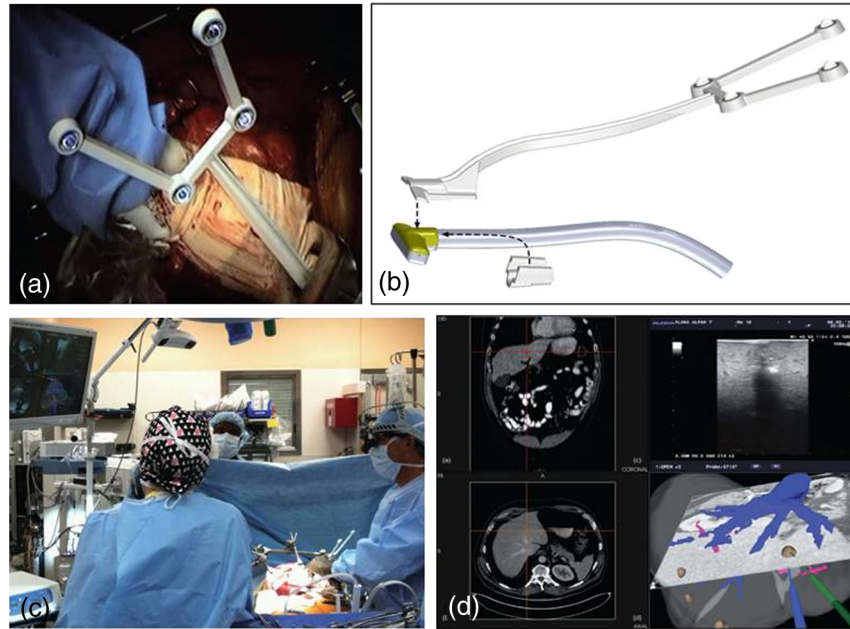


**Fig. 2** (a) The tracked adapter device in use during surgery during the organ interrogation with ultrasound and (b) a schematic of the adapter used to track an Aloka T-probe (UST-5713-T, Hitachi Aloka Medical Ltd., Wallingford, Connecticut) within the Explorer™ Liver navigation system. (c) A view of the OR during the use of the tracked iUS functionality within the Explorer™ Liver navigation system and (d) a screen capture of the Explorer™ Liver navigation system with iUS tracking in use during an ablation probe placement in an open hepatic procedure. Note that the oblique CT slice that corresponds with the tracked iUS plane is displayed in the lower right quadrant of the interface. These images were published in the work of Kingham et al.<sup>16</sup>

substitutions can be made such that Eq. (1) can be restated as a system of partial differential equations (PDEs) in terms of the displacement vector ( $\mathbf{u}$ ) and the Young's modulus ( $E$ ) and Poisson's ratio ( $\nu$ ) material properties

$$\frac{E}{2(1+\nu)} \nabla^2 \mathbf{u} + \frac{E}{2(1+\nu)(1-2\nu)} \nabla(\nabla \cdot \mathbf{u}) = \mathbf{B}. \quad (2)$$

In order to solve the system equations in (2) over the liver mesh domain, the Galerkin weighted residual method is applied using linear basis functions. Using this technique, the system of PDEs reflecting the displacement vectors ( $\mathbf{u}$ ) at each node in the tetrahedral mesh can be compiled in matrix form using the following relation:

$$[K]\{\mathbf{u}\} = \{\mathbf{b}\}, \quad (3)$$

where  $[K]$  is the global stiffness matrix and  $\{\mathbf{b}\}$  is the body force distribution at each node. The driving force generating deformations with an FEM model is provided by the prescription of the appropriate conditions along the boundary of the tetrahedral mesh.

### 2.2.2 Algorithm 1: Laplacian-Based boundary condition specification

The first algorithm tested in this work (described by Dumpuri et al.<sup>9</sup>) drives the biomechanical model by generating a boundary condition set from the closest-point distances between the intraoperative organ surface digitization and the preoperative surface model. Given the fact that the closest-point distances computed between the intraoperative and preoperative organ

surfaces are sparse in nature, displacement boundary conditions can be specified for only a relatively small number of mesh surface nodes. Given the fact that the entire organ surface experiences deformation during surgery, driving the biomechanical model with a sparse set of surface displacements could result in inaccurate predicted deformation fields. Since intraoperative tomographic imaging is not part of the standard of care in open liver surgery, it is not possible to obtain a full characterization of the surface displacements that occur during the intervention. Therefore, this algorithm performs an extrapolation of the sparse closest-point distance measurements (after rigid alignment) over the entire organ surface by solving a Laplace equation on the surface of the undeformed tetrahedral finite element mesh. The method was originally used by Ou et al.<sup>19</sup> within the context of point correspondence determination in nonrigid registration for breast elastography. The extrapolated closest-point distance measurements are used as Dirichlet boundary conditions, specified in a coordinate system that is described by the normal and tangential nodal directions on the undeformed surface, to drive the biomechanical model.

### 2.2.3 Algorithm 2: nonrigid deformation and optimization

As mentioned, the Dirichlet boundary conditions are determined by a “support surface” specified to the posterior region of the organ surface. The support surface is specified via the bivariate polynomial form as follows:

$$\mathbf{u}_s = \hat{\mathbf{n}}_s \sum_{1 \leq i+j \leq n} c_{ij} t_1^i t_2^j, \quad (4)$$

where  $\mathbf{u}_s$  is the displacement vector for a point on the support surface,  $\hat{\mathbf{n}}_s$  is the average normal unit vector over the designated

support region (the area weighted average over the triangular boundary elements), and  $t_1$  and  $t_2$  are the tangential coordinates of the point on the support surface (measured from the origin perpendicular to  $\hat{\mathbf{n}}_s$  in two orthogonal directions). Thus, the constant coefficients  $c_{ij}$  define the nonrigid displacement field over the support region. The sum over  $1 \leq i + j \leq n$  avoids redundancy with the subsequent rigid transformation by excluding the constant displacement mode, which is captured with general rigid body motion.

Using the principle of superposition, it is possible to facilitate rapid computation of model solutions given a combination of support surface coefficients. The model solution for each of the coefficients  $c_{ij}$  is precomputed and stored in matrix  $M$ , where each column is the displacement vector  $u_{ij}$  obtain by solving Eq. (4) where the right-hand side vector is computed with  $c_{ij} = 1$  with all other coefficients set to zero. Therefore, the following equation can be used for rapid model solution computation:

$$\{\mathbf{u}\} = [M]\{\mathbf{c}\}. \quad (5)$$

After generating a model solution for a particular set of polynomial coefficients, the rigid alignment can be updated between the intraoperative surface digitization and the deformed organ model. To achieve this end, a six degrees-of-freedom rigid body transformation can be applied to the deformed nodal coordinates. Therefore, the set of parameters used to generate the total displacement field is as follows:

$$P = \{\mathbf{c}^T, t_x, t_y, t_z, \theta_x, \theta_y, \theta_z\}. \quad (6)$$

The optimal parameter set in Eq. (6) is determined via a Levenberg–Marquardt algorithm such that the following objective function is minimized:

$$F = \frac{1}{N} \sum_{i=1}^N [\hat{\mathbf{n}}_{ci}^T (\mathbf{p}_{di} - \mathbf{p}_{ci})]^2 + \alpha E^2, \quad (7)$$

where  $\mathbf{p}_{di}$  is a  $3 \times 1$  vector containing the Cartesian coordinates for the location of the  $i$ 'th point in the intraoperative sparse surface,  $\mathbf{p}_{ci}$  is the location of the corresponding point on the preoperative organ model surface, generated via the closest-point operator, and  $\hat{\mathbf{n}}_{ci}$  is a unit vector normal to the model surface at  $\mathbf{p}_{ci}$ , and  $N$  is the total number of intraoperative surface points. The energy constraint term ( $E$ ) is proportional to the total strain energy stored in the displacement field produced by the model solution and is calculated as  $E = \mathbf{u}^T \mathbf{K} \mathbf{u}$ . Given that  $\alpha$  is a weighting constant, the term  $\alpha E$  serves as a regularization term for the optimization to balance the distortion of the deformation field. The algorithm is initialized via initial rigid surface alignment between the intraoperative surface digitization and preoperative organ model. The optimization procedure is performed for a fixed number of iterations or until the residual error between the two surfaces reaches a certain threshold.

### 2.3 Retrospective Validation Procedure

Using the liver surface generated from the preoperative tomograms, a tetrahedral mesh of the organ was generated using a customized mesh generator. We employ the algorithm described by Sullivan et al.<sup>20</sup> to generate the tetrahedral liver mesh. After mesh generation, a “support surface” region on the posterior

side of the organ is delineated for the nonrigid correction within Algorithm 2. Both mechanics-based correction algorithms were initialized with the rigid surface registration computed within the Explorer™ Liver guidance system,<sup>17</sup> and the final solution of mesh node displacements was used to deform the 3-D surface models of the patient anatomy generated from the preoperative tomograms. As in the work of Rucker et al.<sup>10</sup>, the value for the energy weighting coefficient ( $\alpha$ ) of  $2 \times 10^{-4}$  and the order of the bivariate polynomial ( $n$ ) of three were used in this work while running Algorithm 2. It should be noted that the value of  $\alpha$  was selected in the work of Rucker et al. based on an empirical evaluation of performance using clinical data and the value of  $n$  was selected based on a sensitivity analysis.

It should be noted that the intraoperative surface digitizations acquired from the tracked LRS device and the tracked stylus were concatenated to maximize the extent of organ coverage for the deformation-correction algorithms. In our experience with a number of clinicians over different open surgeries, there is considerable variability in the size of laparotomy incision employed by a particular clinician and for a particular patient. As such, the extent of organ coverage that can be obtained using the LRS scanner is limited in cases where a small laparotomy incision is employed. The optically tracked stylus design facilitates the acquisition of organ surface regions that cannot be reached by the optical line of sight of the LRS device. Therefore, the optimal intraoperative surface digitization involves a combination of the dense sampled, noncontact LRS data as well as the sparser manual surface digitization, despite the impact of manual acquisition error for the swabbed surface data.

Upon completion of the surgical procedure, a review of the tracked iUS images acquired was performed by the clinician to delineate anatomical structures that would best serve as targets for the deformation-correction evaluation. Based on the clinician review, contour segmentations were performed of the anatomical structures (i.e., vessels) and transformed by both the rigid surface registration computed within the guidance system and the updated rigid surface registration computed within the deformation-correction algorithm. The quantitative error metric used was the mean closest-point distance between the contours segmented in the iUS images and the corresponding 3-D models of the structures generated from the preoperative tomograms. To clarify, the deformed anatomical models were used for the contour-to-model closest-point distance calculation for the deformation-correction evaluation. The contour-to-model closest-point distance target error ( $\bar{E}$ ) metric can be described by the following equation:

$$\bar{E} = \frac{1}{N_{\text{ctr}}} \sum_{i=1}^{N_{\text{ctr}}} \|C_i([T_{\text{reg}}][T_{\text{track}}][T_{\text{cal}}]\mathbf{p}_{\text{ctr},i}, \mathbf{p}_{\text{tar}}) - [T_{\text{reg}}][T_{\text{track}}][T_{\text{cal}}]\mathbf{p}_{\text{ctr},i}\|, \quad (8)$$

where  $N_{\text{ctr}}$  is the number of iUS feature contour points,  $T_{\text{reg}}$  is the physical-to-image space rigid body transform for the alignment method,  $T_{\text{track}}$  is the tracked rigid body transformation,  $T_{\text{cal}}$  is the iUS transducer calibration transformation,  $\mathbf{p}_{\text{tar}}$  is the vector of target anatomical feature points,  $\mathbf{p}_{\text{ctr}}$  is the vector of iUS feature contour points, and  $C$  is the closest-point distance operator.

3 Results

Upon completion of computing the results of the model-based deformation corrections using the two algorithms for the six patients, the surface residual errors after computing the rigid surface-based registration and postcorrection using both algorithms were compiled. The surface residual error refers to the closest-point Euclidean data set computed between the intraoperatively acquired surface digitization and the preoperative organ surface. A summary of the surface residual errors for the six patients is shown in Table 2 and indicates that the surface residual errors values are reduced after the performance of deformation correction using both methods.

Further, Fig. 3 shows the initial rigid registration between each set of acquired data and the preoperative organ using our salient feature registration. With each set in the six pairs, we see the signed closest-point distance map to the closest model data node on the left. We restrict the level of correspondence to a single point in this case to see the nature of the sparseness of measurements. On the right, we see the combined

swabbing and laser range data registered to the preoperative image. The signed closest-point distance texture map was computed as described in the work of Clements et al.<sup>3</sup>

In addition to quantitative metrics, a series of qualitative visualizations are presented to represent the impact of the deformation-correction Algorithm 2 on the alignment of the tracked iUS with the corresponding anatomical features generated from the preoperative tomograms. Figure 4 shows a rendering of the alignment of a tracked iUS image of the left portal vein confluence for patient 1 under conditions of rigid registration and deformation correction. It should be noted that the visualization of the result of the deformation correction involves both the deformed anatomical models and an updated rigid body transform. Additionally, a visualization of the location of the tracked iUS image of the left portal vein confluence using both the rigid surface-based registration and deformation corrected surface and anatomy for patient 2 is shown in Fig. 5. Finally, a visualization of the location of the tracked iUS image of the right hepatic vein using both the rigid surface-based registration and deformation corrected surface and anatomy for patient 3

**Table 2** A summary of the surface residual errors computed between the intraoperative sparse surface and the organ model generated from preoperative tomograms after rigid registration and deformation correction. The surface residual error is the mean closest-point Euclidean distance computed over the intraoperative sparse surface points. The maximum surface closest-point distance is shown in parentheses.

Patient	Rigid registration error (mm)	Algorithm 1 Postcorrection error (mm)	Algorithm 2 Postcorrection error (mm)
1	2.8 ± 2.1 (12.0)	2.5 ± 1.2 (12.1)	2.2 ± 2.1 (15.8)
2	4.8 ± 3.7 (21.1)	3.1 ± 2.0 (17.6)	3.4 ± 2.2 (10.2)
3	4.6 ± 3.6 (17.0)	2.8 ± 1.4 (10.1)	1.9 ± 1.1 (7.0)
4	4.4 ± 3.2 (14.1)	2.9 ± 1.8 (12.0)	4.0 ± 2.7 (13.5)
5	4.3 ± 2.8 (17.8)	2.4 ± 1.3 (13.7)	3.0 ± 2.1 (12.4)
6	4.5 ± 3.0 (14.1)	2.7 ± 1.4 (11.9)	3.1 ± 2.3 (16.4)

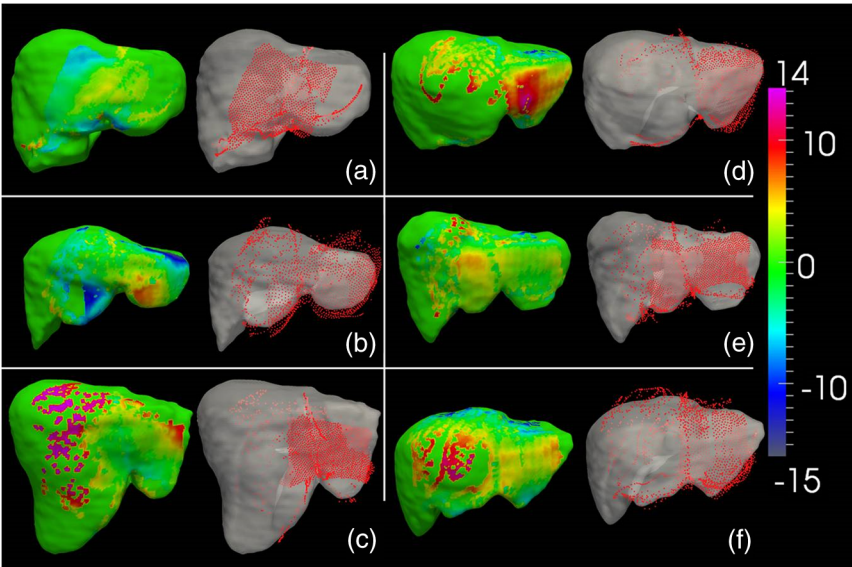


**Fig. 3** Visualization of the rigid registration alignment and texture map of the closest-point distances for the six patient cohort included in the current work. The figure panel labels of (a)–(f) indicate the results for patients 1 to 6, respectively. The six sets of data demonstrate the incidence of significant soft-tissue deformation in open IGLS and highlight the sparse nature of intraoperative liver surface digitization.



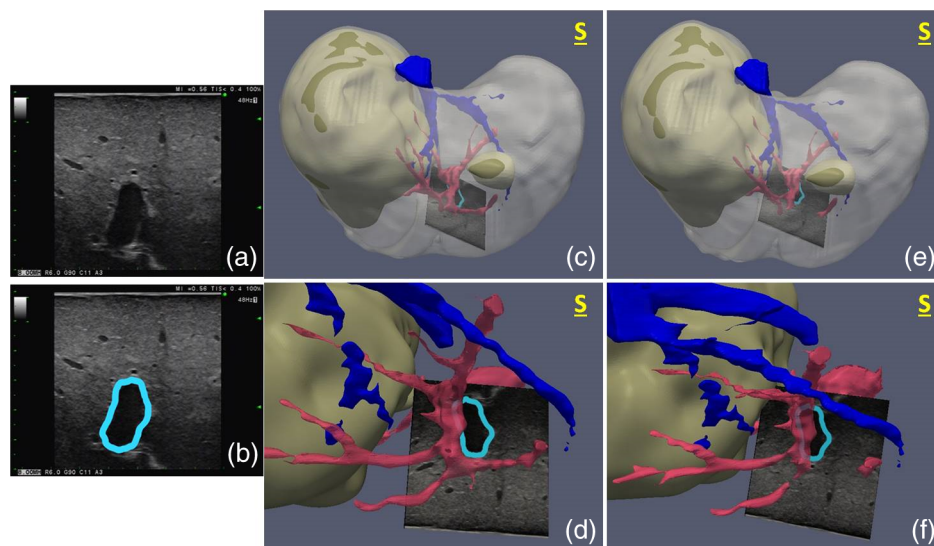


**Fig. 4** Visualization of the tracked iUS image plane rendered within the 3-D models generated from the preoperative tomograms for patient 1. The raw iUS image captures used in the analysis are shown in panel (a) and panel (b) shows the highlighted anatomical feature (i.e., left portal vein confluence). The rigid registration transformation computed during the surgical procedure was used to generate the overlays in panels (c) and (d). Panel (c) shows a superior view of the rigid alignment and includes a rendering of the lesions (brown), hepatic vasculature (blue), portal vasculature (pink), and liver surface (gray). Panel (d) shows a zoomed superior view of the tracked iUS and portal vein structure. The deformed anatomical models and updated transform from the deformation-correction Algorithm 2 were used to generate the renderings in panels (e) and (f). Panel (e) shows a superior view of the deformation corrected alignment and includes a rendering of the lesions (brown), hepatic vasculature (blue), portal vasculature (pink), and liver surface (gray). Panel (f) shows a zoomed superior view of the tracked iUS and portal vein structure after deformation correction.

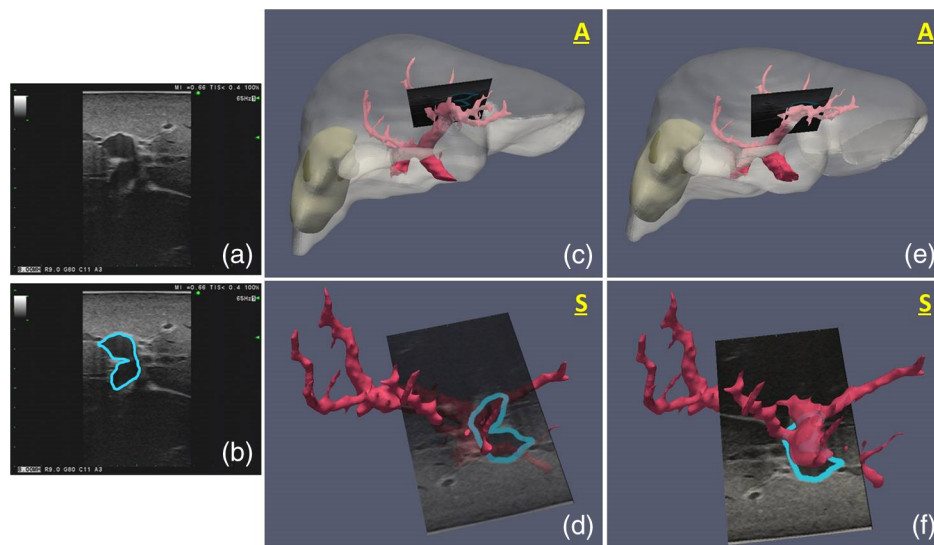


**Fig. 5** Visualization of the tracked iUS image plane rendered within the 3-D models generated from the preoperative tomograms for patient 2. The raw iUS image captures used in the analysis are shown in panel (a) and panel (b) shows the highlighted anatomical feature (i.e., left portal vein confluence). The rigid registration transformation computed during the surgical procedure was used to generate the overlays in panels (c) and (d). Panel (c) shows an anterior view of the rigid alignment and includes a rendering of the lesion (brown), portal vasculature (pink), and liver surface (gray). Panel (d) shows a zoomed superior view of the tracked iUS and portal vein structure. The deformed anatomical models and updated transform from the deformation-correction Algorithm 2 were used to generate the renderings in panels (e) and (f). Panel (e) shows an anterior view of the deformation corrected alignment and includes a rendering of the lesion (brown), portal vasculature (pink), and liver surface (gray). Panel (f) shows a zoomed superior view of the tracked iUS and portal vein structure after deformation correction.



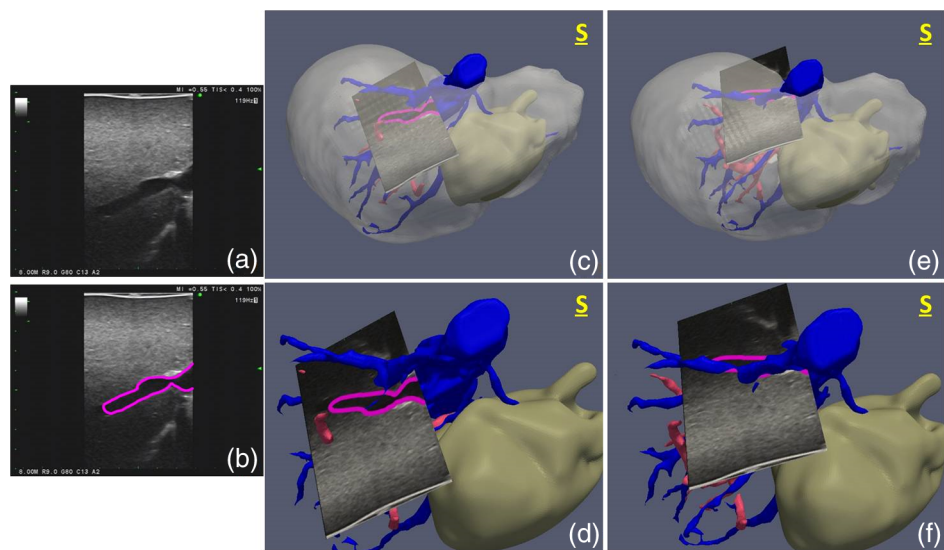


**Fig. 6** Visualization of the tracked iUS image plane rendered within the 3-D models generated from the preoperative tomograms for patient 3. The raw iUS image captures used in the analysis are shown in panel (a) and panel (b) shows the highlighted anatomical feature (i.e., right hepatic vein). The rigid registration transformation computed during the surgical procedure was used to generate the overlays in panels (c) and (d). Panel (c) shows a superior view of the rigid alignment and includes a rendering of the lesion (brown), portal vasculature (pink), hepatic vasculature (blue), and liver surface (gray). Panel (d) shows a zoomed superior view of the tracked iUS and hepatic vein structure. The deformed anatomical models and updated transform from the deformation-correction Algorithm 2 were used to generate the renderings in panels (e) and (f). Panel (e) shows a superior view of the deformation corrected alignment and includes a rendering of the lesion (brown), portal vasculature (pink), hepatic vasculature (blue), and liver surface (gray). Panel (f) shows a zoomed superior view of the tracked iUS and hepatic vein structure after deformation correction.

is shown in Fig. 6. Qualitatively, the alignment between the iUS image of the vascular structures and the preoperative model is substantially improved by the deformation-correction algorithm in the three patients.

Finally, a summary of the contour-to-model closest-point distance measurements for the eight anatomical subsurface targets

across the six clinical cases where deformation correction was performed using Algorithms 1 and 2 are shown in Tables 3 and 4, respectively. As shown, the deformation-correction method of Algorithm 2 appears to improve registration accuracy by ~52%. In contrast, the evaluation of Algorithm 1 (shown in Table 3) indicates a more modest improvement of ~10% on average.

**Table 3** Summary of the contour-to-model closest-point distance errors between homologous features delineated in the preoperative tomograms and the tracked iUS image sets under conditions of rigid registration and postdeformation correction driven by Algorithm 1. The maximum contour-to-model closest-point distance is shown in parentheses. A mean shift correction measurement is also presented for each feature to provide a sense of the efficacy of the model-based correction algorithm.

Patient	Anatomical feature	Rigid registration error (mm)	Postcorrection error (mm)	Shift correction (%)
1	Left portal vein confluence	5.2 ± 3.1 (11.9)	5.5 ± 3.5 (13.0)	(5.8)%
1	Left hepatic vein	6.2 ± 1.5 (8.8)	6.8 ± 1.9 (9.7)	(9.7)%
2	Left portal vein confluence	4.9 ± 3.1 (10.0)	2.8 ± 2.0 (7.8)	42.9%
3	Right hepatic vein	4.6 ± 2.8 (11.3)	5.2 ± 3.2 (11.2)	(13.0)%
4	Portal vein confluence	6.2 ± 2.9 (10.7)	2.5 ± 1.4 (5.6)	59.7%
4	Right hepatic vein	10.0 ± 2.7 (14.9)	6.3 ± 3.4 (12.5)	37.0%
5	Segment III portal pedicle	5.5 ± 2.6 (10.9)	8.7 ± 2.5 (12.4)	(58.2)%
6	Segment IVb pedicle	2.2 ± 1.2 (5.2)	2.0 ± 1.1 (4.2)	9.1%
Mean		5.6 ± 2.2	5.0 ± 2.3	10.7% <sup>a</sup>

<sup>a</sup>Note that this value represents the shift correction percentage computed directly from the mean rigid registration and postcorrection errors and not a direct computation of the mean shift correction percentages.

**Table 4** Summary of the contour-to-model closest-point distance errors between homologous features delineated in the preoperative tomograms and the tracked iUS image sets under conditions of rigid registration and postdeformation correction driven by Algorithm 2. The maximum contour-to-model closest-point distance is shown in parentheses. A mean shift correction measurement is also presented for each feature to provide a sense of the efficacy of the model-based correction algorithm.

Patient	Anatomical feature	Rigid registration error (mm)	Postcorrection error (mm)	Shift correction (%)
1	Left portal vein confluence	$5.2 \pm 3.1$ (11.9)	$2.5 \pm 1.2$ (5.0)	51.2%
1	Left hepatic vein	$6.2 \pm 1.5$ (8.8)	$1.0 \pm 0.5$ (2.1)	83.9%
2	Left portal vein confluence	$4.9 \pm 3.1$ (10.0)	$2.0 \pm 1.2$ (4.9)	59.2%
3	Right hepatic vein	$4.6 \pm 2.8$ (11.3)	$2.0 \pm 1.3$ (5.4)	56.5%
4	Portal vein confluence	$6.2 \pm 2.9$ (10.7)	$4.3 \pm 2.9$ (9.9)	30.6%
4	Right hepatic vein	$10.0 \pm 2.7$ (14.9)	$4.5 \pm 2.7$ (9.8)	55.0%
5	Segment III portal pedicle	$5.5 \pm 2.6$ (10.9)	$2.4 \pm 1.5$ (5.4)	56.4%
6	Segment IVb pedicle	$2.2 \pm 1.2$ (5.2)	$2.5 \pm 1.6$ (5.7)	(13.6)%
MEAN		$5.6 \pm 2.2$	$2.7 \pm 0.7$	51.8% <sup>a</sup>

<sup>a</sup>Note that this value represents the shift correction percentage computed directly from the mean rigid registration and postcorrection errors and not a direct computation of the mean shift correction percentages.

The contrast between the impact of the deformation correction on the surface residual metrics presented in Table 2 and the subsurface contour-to-model distances is notable over this patient cohort. In particular, Algorithm 2 does not have as great an impact on reducing the surface residual errors, yet has a much greater impact on the reduction of the subsurface contour-to-model target errors.

## 4 Discussion

The results presented represent the first effort to evaluate biomechanical model-based deformation-correction algorithms for IGLS driven by sparse surface data using clinically acquired subsurface anatomical targets. It should be noted that previous work by Beller et al.<sup>6</sup> has employed a validation technique using clinical data for their spline-based deformation-correction algorithm. The work presented here is differentiated due to the fact that the subsurface anatomical targets used in the algorithm validation were completely segregated from the sparse data and not used to drive the model. In other words, the model-based deformation-correction algorithm employed in this work was driven solely by sparse surface data acquired intraoperatively, while the validation metrics were computed using subsurface anatomical targets digitized via tracked iUS.

The visualizations (shown in Figs. 4, 5, and 6) of the impact of the deformation-correction algorithm on tracked iUS alignment indicates that the proposed algorithm provides a substantial correction for the soft-tissue deformation encountered during these procedures. Additionally, the quantitative summary of the subsurface contour-to-model distance errors (shown in Table 4) indicates that the correction of Algorithm 2 can compensate for ~52% of the encountered soft-tissue shift and represents an improvement over the correction results shown for Algorithm 1. The contour-to-model distance errors shown in Table 3 indicate that Algorithm 1 is significantly less robust with respect to correcting subsurface target errors as compared with Algorithm 2. It should be noted that while Algorithm 2 resulted in a larger contour-to-model target error in case 5

than reported for the condition of rigid registration, the low absolute value of the target error indicates that, while the surface deformation was similar to other cases, there was likely minimal detectable soft-tissue deformation for this particular target.

In addition to, reporting the subsurface contour-to-model distance metrics in Tables 3 and 4, the surface residual error metrics have also been presented in Table 2 for reference. It is interesting to note that Algorithm 2 outperforms Algorithm 1 on six of eight target errors (six of seven if one does not consider the small target error comparison of case 5). However, in Table 2, which compares surface fit, Algorithm 1 outperforms Algorithm 2 in four of six cases. This is an interesting result and implies that it is critical for validation work to evaluate both surface and subsurface residual error metrics to really capture performance of deformation-correction algorithms. In addition, we can also glean some insight from this result based on the methodologies employed by each algorithm. Algorithm 1 is a direct surface residual fit algorithm with an attempt to extrapolate information from that visible data region to nonvisible regions of the organ. In contrast, Algorithm 2 attempts to reconstruct backside liver deformations to best fit the visible surfaces. Fundamentally, these represent very different modes of enforcing fit on the domain and the results would suggest that the supportive backside deformation reconstruction is a more accurate representation of the actual deformations imposed during the surgical procedure and facilitates greater reductions with respect to subsurface target error.

In summary, the clinical validation presented within the evaluation of previously proposed deformation-correction techniques for open liver image-guidance have largely relied on surface-based metrics and phantom experiments have been used for the characterization of subsurface target accuracy. The proposed method represents a significant advancement in methodology for the evaluation of deformation correction in open hepatic surgical navigation via the use of independent subsurface anatomical targets acquired during clinical procedures for validation. While further refinement

in deformation-correction methodology is needed, the average error correction of 52% facilitated by Algorithm 2 represents a meaningful advancement toward the realization of a model-updated surgical navigation system for open liver resection.

## 5 Conclusions

The preliminary results indicate that the proposed validation method is promising in facilitating the refinement of deformation-correction algorithms for image-guidance systems used in open liver procedures. The evaluation indicates that deformation-correction methods are available that are capable of compensating for ~52% of the soft-tissue deformation that is experienced during open liver procedures. Future work will involve the generation of 3-D models of the anatomical structures acquired via the tracked iUS framework to facilitate the computation of more descriptive target error metrics and the methods of Pheiffer et al. to correct for the impact of tissue compression from the iUS transducer.<sup>21</sup> Additionally, future work will also involve use of the subsurface tracked iUS data to validate further refinement of Algorithm 2 via incorporation of salient anatomical feature weighting that is used in the rigid surface-based registration algorithm used in the Explorer™ Liver guidance system.

## Acknowledgments

This work was supported under the NIH grant R01-CA162477. Many of the algorithms and visualization tools used in this work were developed using the Visualization Toolkit ([www.vtk.org](http://www.vtk.org)) and MATLAB (The MathWorks, [www.themathworks.com](http://www.themathworks.com)). The FastRBF Toolkit (FarField Technology, Christchurch, NZ) was used to generate a number of the surfaces shown. The ANN Nearest Neighbor Search Library was used to speed up closest-point searches. ParaView 3.98.1 ([www.paraview.org](http://www.paraview.org)) was used to generate a number of rendered surface screen captures shown.

## References

- O. Heizmann et al., "Assessment of intraoperative liver deformation during hepatic resection: prospective clinical study," *World J. Surg.* **34**, 1887–1893 (2010).
- D. M. Cash et al., "Concepts and preliminary data toward the realization of image-guided liver surgery," *J. Gastrointest. Surg.* **11**, 844–859 (2007).
- L. W. Clements et al., "Organ surface deformation measurement and analysis in open hepatic surgery: method and preliminary results from 12 clinical cases," *IEEE Trans. Biomed. Eng.* **58**, 2280–2289 (2011).
- O. F. Bathe et al., "Complex hepatic surgery aided by a 1.5-tesla moveable magnetic resonance imaging system," *Am. J. Surg.* **191**, 598–603 (2006).
- S. S. Chopra et al., "Imaging sequences for intraoperative MR-guided laparoscopic liver resection in 1.0-T high field open MRI," *Eur. Radiol.* **19**, 2191–2196 (2009).
- S. Beller et al., "Feasibility of navigated resection of liver tumors using multiplanar visualization of intraoperative 3-dimensional ultrasound data," *Ann. Surg.* **246**, 288–294 (2007).
- M. I. Miga et al., "Intraoperative registration of the liver for image-guided surgery using laser range scanning and deformable models," *Proc. SPIE* **5029**, 350–359 (2003).
- D. M. Cash et al., "Compensating for intraoperative soft-tissue deformations using incomplete surface data and finite elements," *IEEE Trans. Med. Imaging* **24**, 1479–1491 (2005).
- P. Dumpuri et al., "Model-updated image-guided liver surgery: preliminary results using surface characterization," *Prog. Biophys. Mol. Biol.* **103**, 197–207 (2010).
- D. Rucker et al., "A mechanics-based nonrigid registration method for liver surgery using sparse intraoperative data," *IEEE Trans. Med. Imaging* **33**, 147–158 (2014).
- T. Lange et al., "3D ultrasound-CT registration of the liver using combined landmark-intensity information," *Int. J. CARS* **4**, 79–88 (2009).
- M. Nakamoto et al., "Recovery of respiratory motion and deformation of the liver using laparoscopic freehand 3D ultrasound system," *Med. Image Anal.* **11**, 429–442 (2007).
- S. Li et al., "Development of preoperative liver and vascular system segmentation and modeling tool for image-guided surgery and surgical planning," *Proc. SPIE* **6918**, 69180C (2008).
- B. J. DuBray, "Novel three-dimensional imaging technique improves the accuracy of hepatic volumetric assessment," *HPB* **13**, 670–674 (2011).
- T. S. Pheiffer et al., "Design and evaluation of an optically-tracked single-CCD laser range scanner," *Med. Phys.* **39**, 636–642 (2012).
- T. P. Kingham et al., "Image-guided liver surgery: intraoperative projection of computed tomography images utilizing tracked ultrasound," *HPB* **14**, 594–603 (2012).
- L. W. Clements et al., "Robust surface registration using salient anatomical features for image-guided liver surgery: algorithm and validation," *Med. Phys.* **35**, 2528–2540 (2008).
- T. K. Chen et al., "A real-time freehand ultrasound calibration system with automatic accuracy feedback and control," *Ultrasound Med. Biol.* **35**, 79–93 (2009).
- J. J. Ou et al., "Evaluation of 3D modality-independent elastography for breast imaging: a simulation study," *Phys. Med. Biol.* **53**, 147–163 (2008).
- J. M. Sullivan, G. Charron, and K. D. Paulsen, "A three-dimensional mesh generator for arbitrary multiple material domains," *Finite Elem. Anal. Des.* **25**, 219–241 (1997).
- T. S. Pheiffer et al., "Model-based correction of tissue compression for tracked ultrasound in soft tissue image-guided surgery," *Ultrasound Med. Biol.* **40**, 788–803 (2014).

Biographies for the authors are not available.